www.czasopisma.pan.pl PAN POLSKA AKADEMIA NAUK www.journals.pan.pl

Arch. Metall. Mater. **67** (2022), 1, 17-30

DOI: https://doi.org/10.24425/amm.2022.137467

HAITAO XUE[1], XIAOPING LUAN[1*], WEIBING GUO[1], DONG ZHOU[1]

MICROSTRUCTURE AND PROPERTIES OF TIG SURFACING Co-BASED ALLOY ON UMCo50 PROCESS BURNER

The surfacing layer of cobalt-based alloy is prepared using the tungsten inert gas welding (TIG) process and employing the UMCo50, ST1 and ST6 filler materials. The metallographic testing, hardness, wear and corrosion testing of different surfacing layers have been carried out. Each area of the surfacing layer is characterized using the optical and scanning electron microscope (SEM). Cellular and a few columnar dendrites have been observed near the fusion line of the UMCo50 surfacing layer, and cellular structure is observed in the central region. Dendrites and cellular crystals have been observed in the ST1 and ST6 surfacing layers. The average hardness of UMCo50, ST1 and ST6 surfacing layers are 320 HV, 672.3 HV and 497.5 HV, respectively. The wear loss of the ST1, ST6 and UMCo50 surfacing layer is 2.71 mg, 4.35 mg, and 14.57 mg, respectively. The corrosion weight loss of the ST1, ST6 and UMCo50 surfacing layers are 0.0388 g, 0.0477 g and 0.0833 g, respectively.

Keywords: UMCo50 alloy; surfacing; microstructure; properties

1. Introduction

With the rapid development of the global economy, energy consumption is increasing, and the global energy structure has begun to transform. Due to the lack of natural gas and oil resources, coal will continue to be the dominant energy source for a long time [1]. The direct combustion of coal will produce a large number of polluting gases and dust particles, which pollute the environment. Also, the inadequate combustion of coal will lead to low energy efficiency, and the comprehensive utilization efficiency is about 60%. Therefore, the development of new clean coal technology and the improvement of coal resources combustion efficiency are an important method to solve this problem [2-4].

Coal water slurry gasification technology is a new clean coal technology in recent years, it is mainly used in chemical, power generation, metallurgy fields [5-7]. It uses coal and water as raw materials, and mixes them to make coal water slurry by adding fixed proportions of chemical additives. As a clean energy source to replace oil and natural gas, coal water slurry has the advantages of convenient storage and transportation, good fluidity, and sufficient combustion [8-10]. The process burner is the core device of the coal water slurry gasification technology, and its function is to make the coal water slurry and oxygen enter the gasifier for full combustion. Due to the erosion of combustion products and the influence of high temperature airflow, cracks will appear on the outer end face of the process burner after a period of service, which will reduce the service life and work efficiency and seriously threaten the safety of the equipment.

Process burner in the industrial field is generally forged with UMCo50, which is expensive. Due to complex working conditions, its service time is only 90~200 days. In order to save cost and improve efficiency, it is generally necessary to repair the outer end face of the failed burner and put it into use again. Xue et al. [11] reported that T800 cobalt-based alloy powder is surfacing on the UMCo50 substrate. It is found that there are more Laves phases in the surfacing layer, which is beneficial to improve the hardness and wear resistance of the surfacing layer. However, due to the higher content of Mo and lower content of Cr in the surfacing alloy, the corrosivity of the surfacing layer is reduced. Mutascu et al. [12] reported that ST6 welding wire is surfacing on the X2CrNiMoN22-5-3 duplex stainless steel. The hardness test results shown that the surface hardness value is 358~401HV. Hou et al. [13] reported that cobalt-based alloys with different Y_2O_3 content are surfacing on the Q235A-carbon steel. When the content of Y_2O_3 is less than 0.8wt.%, the addition of Y_2O_3 can refine the microstructure and increase the wear resistance properties. However, further increased of its contents

[1] HEBEI UNIVERSITY OF TECHNOLOGY, SCHOOL OF MATERIALS SCIENCE AND ENGINEERING, NO. 5340, XIPINGDAO ROAD, BEICHEN DISTRICT, TIANJIN, 300401, PR CHINA

* Corresponding author: luanxiaoping@126.com

will lead to the agglomeration of undissolved Y_2O_3 particles and lead to a coarse microstructure and lower wear resistance properties. Yao et al. [14] reported three types of cobalt-based alloys are surfacing on the 316 stainless steel plates. The hardness of the ST21, ST22 and ST728 surfacing layers are 35HRC, 41HRC and 44HRC. The ST22 hardfacing is the best and the ST728 hardfacing is the worst in resistance to 3.5% NaCl solution corrosion.

In the present study, the tungsten inert gas welding (TIG) is used to surfacing UMCo50, ST1, and ST6 filler materials on UMCo50 base metal. The microstructure and properties of the surfacing layers are analyzed.

2. Materials and Methods

The round UMCo50 alloy of 120 × 6 mm is used as the base material, the specific chemical composition is shown in Table 1. The surfacing materials are ST1, ST6 and UMCo50 welding wires, the chemical composition is shown in Table 2. Three kinds of welding wires are surfacing on the UMCo50 substrate by Tungsten inert gas (TIG) welding, the welding process is shown in Table 3. The welding equipment is YC-300WX TIG welding machine produced by Panasonic. After the welding test, an X-ray inspection will be carried out on all surfacing layers. The X-ray inspection equipment is UNF series produced by Unicomp. The results show that the surfacing layers are well formed and no internal defects such as cracks, inclusions, and pores, as shown in Figure 1.

The sample with the size of 10 × 10 × 5 mm is cut from the surfacing layer by wire electrical discharge cutting machine, then use 120#, 240#, 400#, 600#, 800#, 1000#, 1500# sandpaper to polish the sample. Then, the sample is polished on the polishing machine with a W1.5 diamond polishing agent until there are no scratches on the surface of the sample. The corrosion agent ($5gCuCl_2$ + $5gFeCl_2$ + $20mLHNO_3$ + 80mLHCl) is used to corrode the sample, and the corrosion time is controlled within 15~30 seconds.

The microstructure of the surfacing layer is analyzed using a universal metallographic analyzer (DM2700) and a scanning electron microscope (JSM-6510). The phases of the surfacing layer are identified by X-ray diffractometer (Druker D8 Discover). The hardness of the surfacing layer is tested by the HMV-2T microhardness tester. The high temperature wear is tested by the high temperature wear tester (MG-2000), the loading force is 100 N, the test temperature is 650°C, the speed is 240 rp, the type of wear test is pin on disk, the material of the

TABLE 1

Chemical composition of the UMCo50 alloy (wt.%)

Co	Cr	Ni	Fe	C	Mn	Si	P	S
48~52	23~29	4.5	15	0.05~0.12	0.5~1.0	0.5~1.0	≤0.02	≤0.0015

TABLE 2

Chemical composition of cobalt-based alloy welding wire (wt.%)

Welding wire	Cr	Ni	W	Fe	Mo	C	Mn	Si	S	P	Co
ST1	29	3	12.5	3	1	2.5	1.0	1.2	—	—	Bal
ST6	27	3	4.5	3	1	1.2	1.0	3	—	—	Bal
UMCo50	23	3	—	17	—	0.05~0.12	≤1.0	≤1.0	≤0.015	≤0.02	Bal

TABLE 3

Welding parameters

Welding wire	Welding current, (A)	Interpass temperature, (°C)	Surfacing speed, (cm/min)	Number of surfacing layers
ST1	140~150A	400	12	2
ST6	140~150A	250	12	2
UMCo50	120~130A	60	12	2

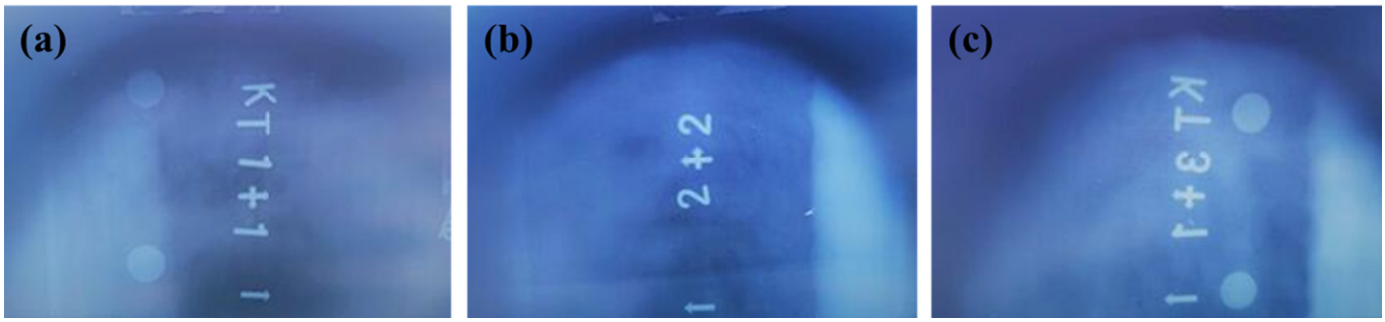

Fig. 1. X-ray inspection of hardfacing layer: (a) UMCo50, (b) ST1, (c) ST6

disc is GCr15, and the test time is 30 minutes. The hot corrosion of the surfacing layer is tested by heat treatment furnace (HMX1600-30), the corrosion medium is 75wt.%Na_2SO_4 + 25wt.%NaCl saturated salt solution, the corrosion temperature is 1000°C, and the corrosion time is 100 hours.

3. Results and Discussion

3.1. Microstructure of Surfacing Layer

The microstructure of the surfacing layer is shown in Figure 2. It can be found that the surfacing material is well combined with the UMCo50 base material. There are no obvious holes and cracks on both sides of the fusion line. The crystal grain of the surfacing layer is grown in the form of epitaxial solidification, and the growth direction is mostly perpendicular to the fusion line.

The microstructure of the UMCo50 surfacing layer is shown in Figure 2(a) and 2(b). The weld metal near the fusion line is characterized by cellular and a few columnar dendrites (Fig. 2(a)). The center region of the weld metal shows the cellular structure with solidified grain boundaries (SGBs), solidified sub-grain boundaries (SSGBs) and migrated grain boundaries (MGBs), and the element segregation along the boundaries (SGBs and SSGBs) is shown in Figure 2(b). The microstructure of the ST6 surfacing layer is shown in Figure 2(c) and 2(d). Near the fusion boundary, solidification mainly occurs in a dendrite mode, and columnar dendrites with clear branches and a small

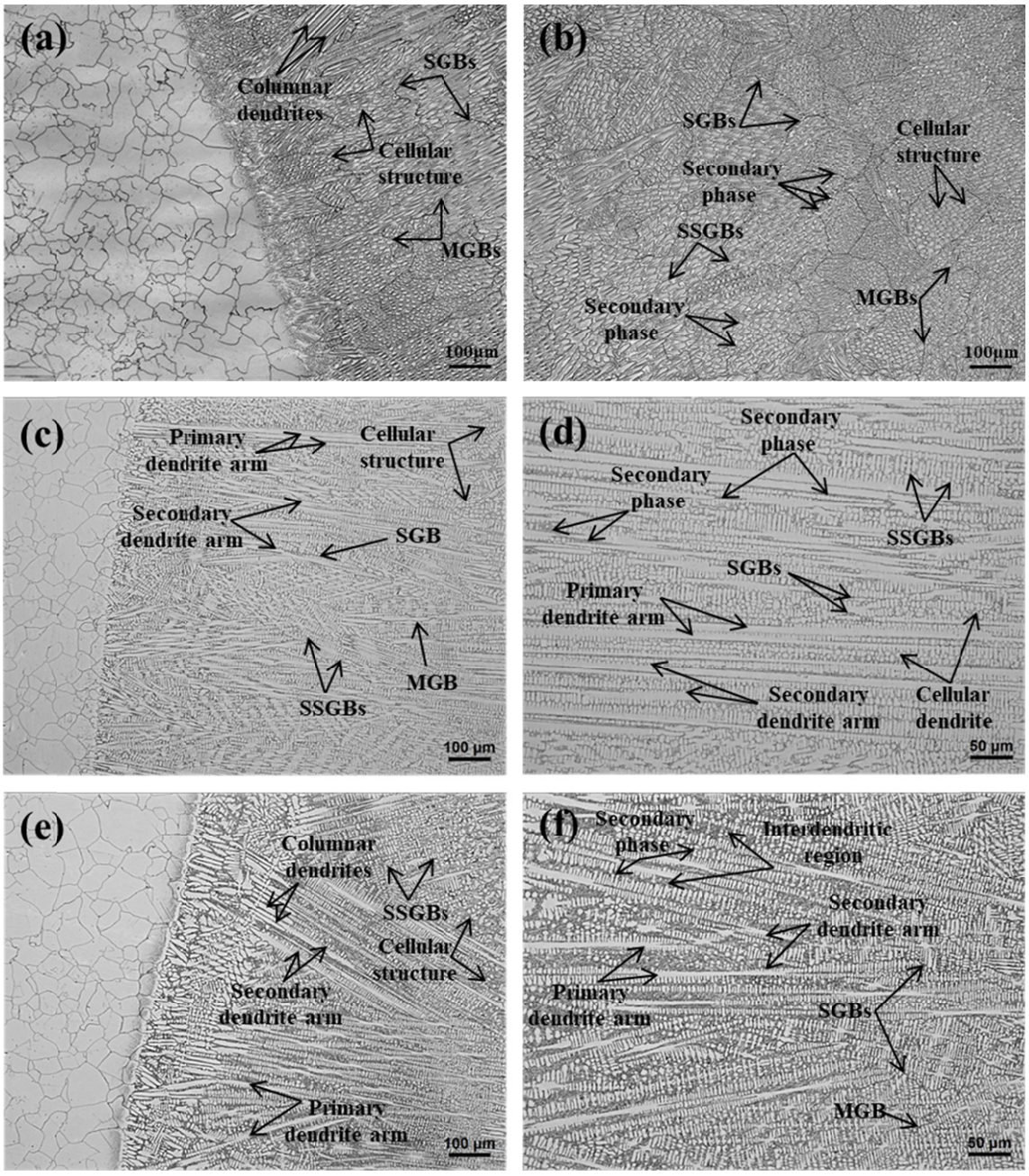

Fig. 2. Metallographic structure: (a) near the fusion line of UMCo50, (b) center of UMCo50 surfacing layer, (c) near the ST6 fusion line, (d) center of the ST6 surfacing layer, (e) near the ST1 fusion line, (f) center of the ST1 surfacing layer

amount of cellular structure are observed, as shown in Figure 2(c). In the central area of the weld metal, primary dendrites, secondary dendrites, inter-dendritic regions with secondary phase precipitates and cellular dendrites can be clearly observed, as shown in Figure 2(d). The microstructure of the ST1 surfacing layer is shown in Figure 2(e) and 2(f). At the interface region, weld fusion zone shows the columnar grain growth, as shown in Figure 2(e). The center of the weld metal shows the primary and secondary dendrites and inter-dendritic areas (Fig. 2(f)). The segregation of the elements along the boundaries and inside the inter-dendritic region is also observed. The direction of crystal grain growth is generally opposite to the direction of heat dissipation. During the cladding process, the heat dissipation direction of the surfacing layer is mainly along the direction of the base material, so the dendrite is mostly grown in the direction perpendicular to the fusion line [15].

Figure 3 shows the X-ray diffraction analysis results of the surfacing layer. It can be seen that the phases of the surfacing layer are α-Co (fcc) and ε-Co (hcp). When the temperature is lower than 417°C, the α-Co→ε-Co phase transition will occur, and this transformation is relatively slow. The Cr element in the surfacing alloy can increase the martensite transformation temperature and stabilize the existence of ε-Co [16,17]. Therefore, there are both α-Co and ε-Co in the surfacing layer after welding.

Figure 4 shows the line mapping of the region between the UMCo50 filler metal and UMCo50 base metal. The line scan chemical composition analysis shows the difference in composition between the weld metal and base metal. It can be seen that the increases in weight percentage of Ni and Si and decrease in weight percentage of the Fe as move from the weld metal to UMCo50 base metal. The line mapping between the ST6 filler metal and the substrate is shown in Figure 5. When moving from the filler metal to the substrate side, the weight percentages of Fe and Ni increase, and the weight percentages of Si, Cr, C, and W decrease. The line mapping between the ST1 filler metal and the substrate is shown in Figure 6. The interface of weld

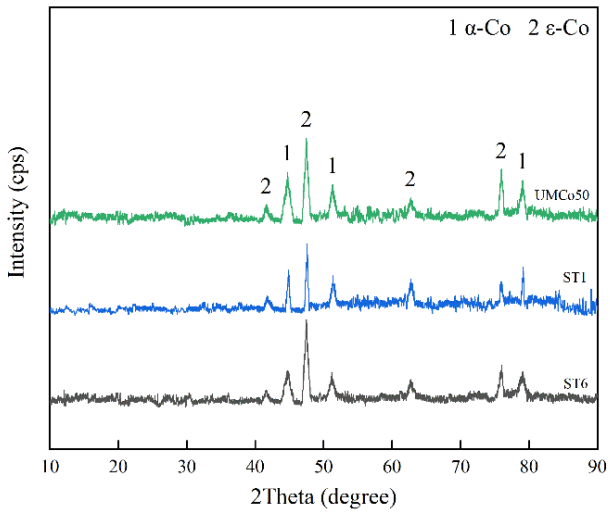

Fig. 3. X-ray diffraction patterns of surfacing layer

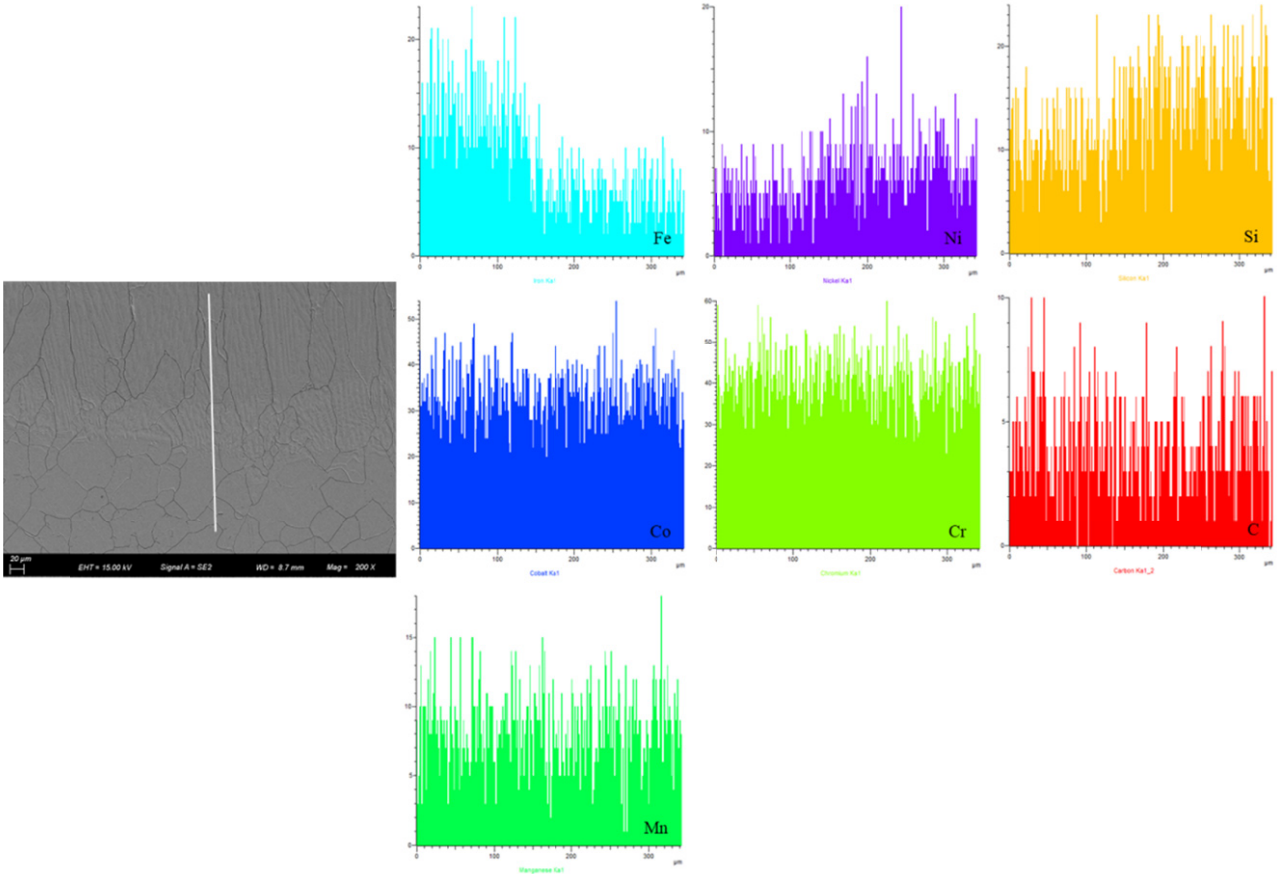

Fig. 4. Line mapping analysis of the interface between UMCo50 filler metal and UMCo50 base metal

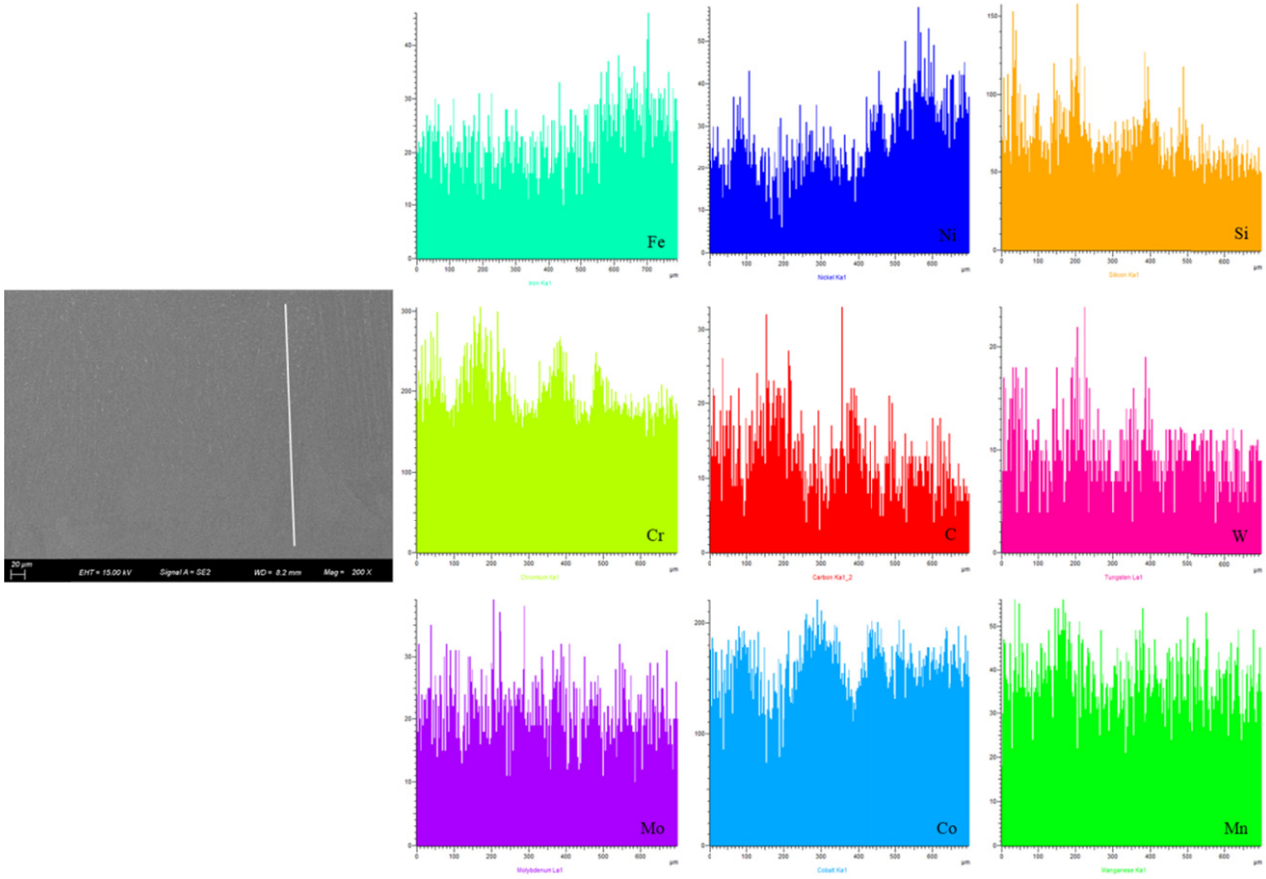

Fig. 5. Line mapping analysis of the interface between ST6 filler metal and UMCo50 base metal

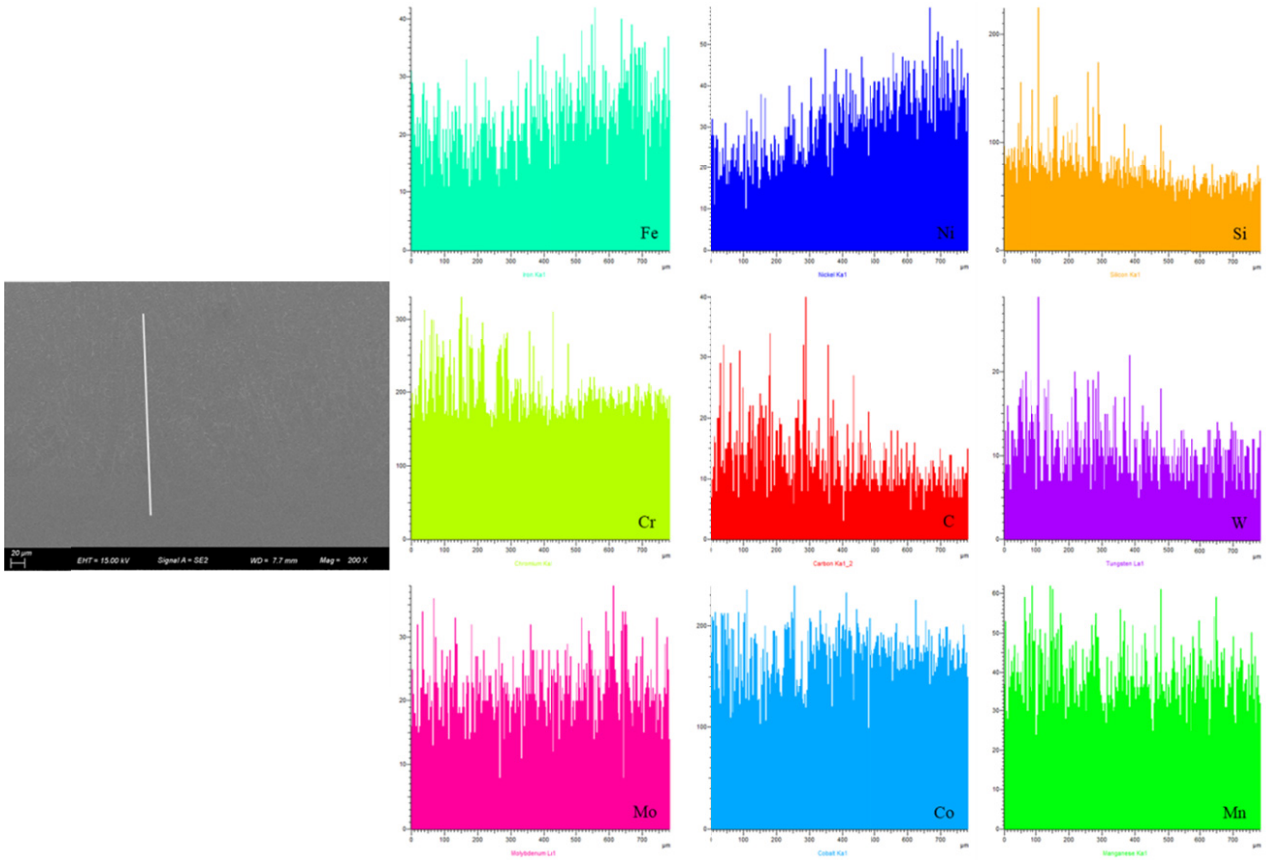

Fig. 6. Line mapping analysis of the interface between ST1 filler metal and UMCo50 base metal

metal and UMCo50 base metal shows the variation in weight percentages of Fe, Ni, Si, Cr, C and W. The line map shows the increases in weight percentage of Fe and Ni, and decreases in weight percentage of the Si, Cr, C and W as move from the weld metal to UMCo50 base metal side.

The center region of the UMCo50 filler metal is shown in Figure 7 at different magnifications. Figure 7(a) shows the cellular crystals along with the segregation of elements at the boundaries. The segregation of the alloying elements along the boundaries is observed very clearly in Figure 7(b). The EDS analysis results of each spot marked in Figure 7(b) are listed in Table 4. The EDS spectra (point 1 and 2) confirm that the segregation of elements like C, Si and Cr. From these results, the precipitates could be inferred as $M_{23}C_6$ and M_7C_3 carbides.

The morphology of the ST6 filler metal is shown in Figure 8. Dendrite core and segregation of elements at the boundaries are shown in Figure 8(a). The chemical composition of each point in Figure 8(b) is measured with by EDS, and the results are shown in Table 5. The EDS analysis confirms the major segregation of the C, Si, Cr, Mo and W along the boundaries. The precipitates could be inferred as $M_{23}C_6$, M_7C_3 and MC carbides.

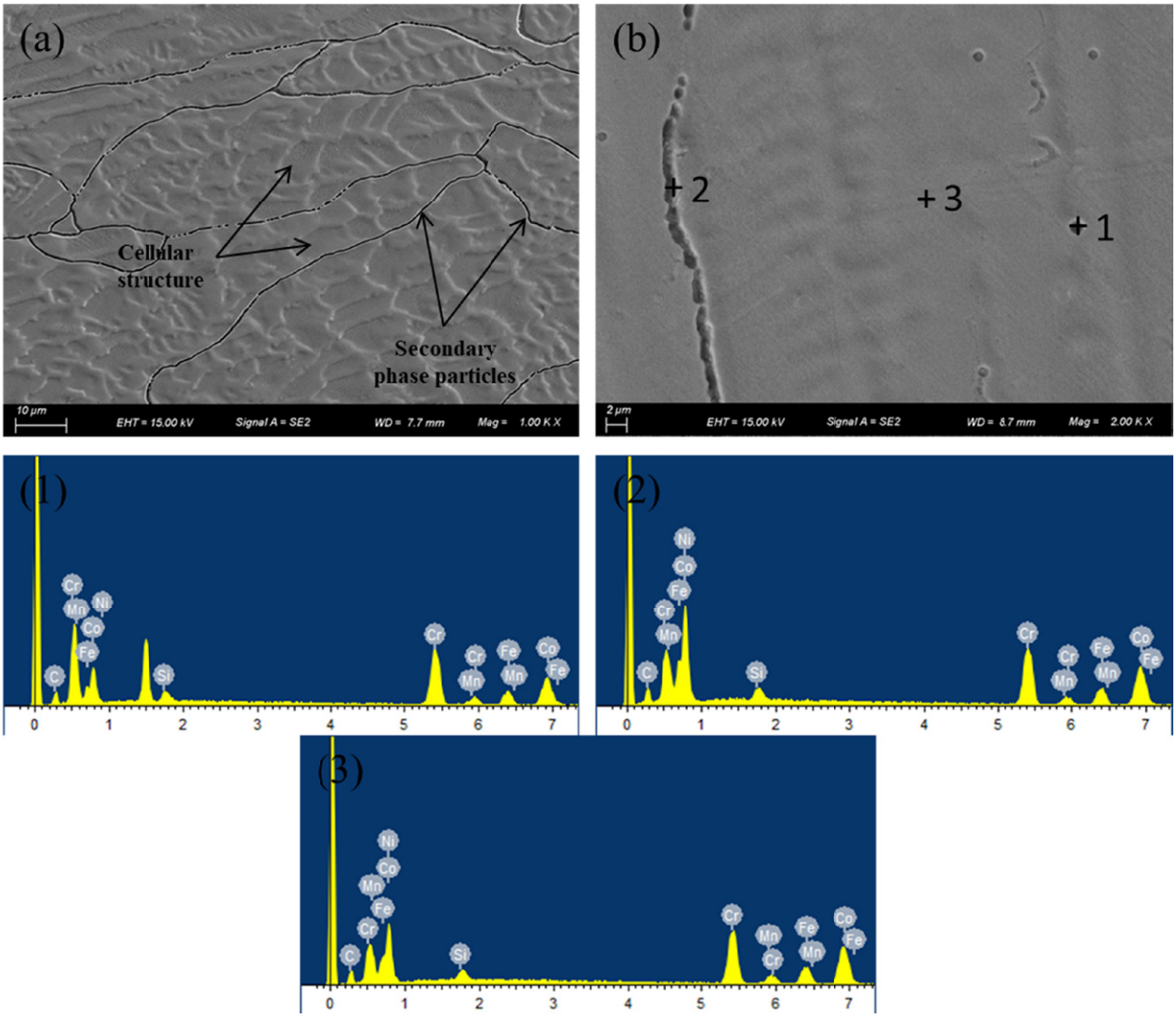

Fig. 7. (a) SEM image of the UMCo50 filler metal center at low magnification, (b) at high magnification showing the location for elemental composition analysis at the boundary

TABLE 4

EDS analysis results of each spot in Fig.7(b) (wt.%)

Point	C	Si	Cr	Mn	Fe	Co	Ni
1	7.24	1.39	33.90	1.76	13.07	40.26	2.37
2	8.20	1.28	29.70	1.62	13.55	43.67	1.98
3	4.82	0.97	23.15	1.84	15.23	49.76	4.23

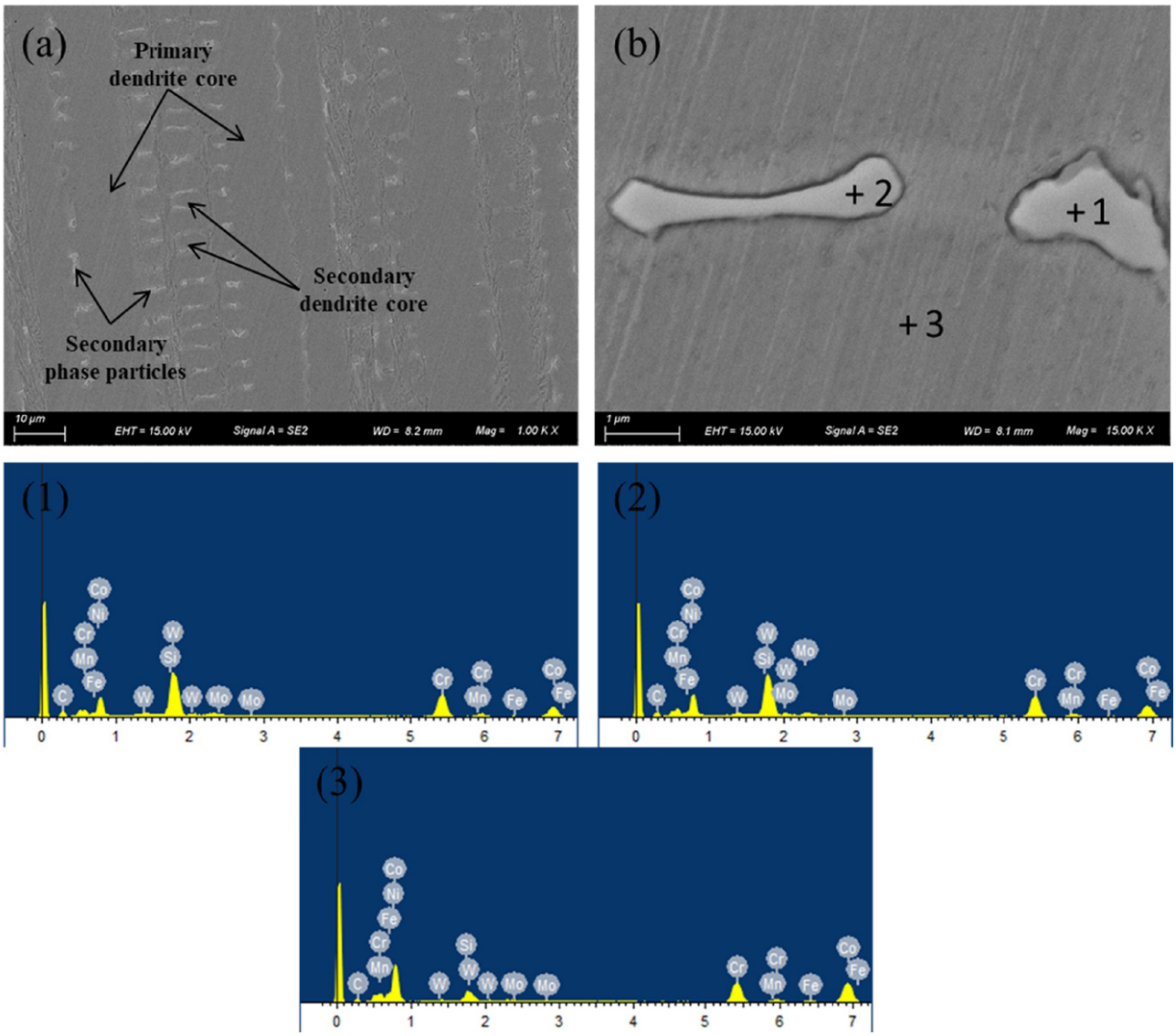

Fig. 8. (a) SEM image of the ST6 filler metal center at low magnification, (b) at high magnification showing the location for elemental composition analysis at the boundary

TABLE 5

EDS analysis results of each spot in Fig. 8(b) (wt.%)

Point	C	Si	Cr	Mn	Fe	Co	Ni	Mo	W
1	8.33	3.47	33.96	1.17	1.31	30.03	1.58	2.38	17.78
2	8.88	3.45	45.44	0.94	1.12	24.61	2.13	2.02	11.40
3	5.37	1.84	24.43	1.32	3.41	53.43	2.96	0.67	6.57

The morphology of the ST1 filler metal is depicted in Figure 9(a), which shows the dendritic core and the segregation of elements in the weld metal. The EDS chemical compositions of each spot in Figure 9(b) are listed in Table 6. The EDS analysis confirms the major segregation of the C, Si, Cr, Mo and W along the boundaries. The weight percentage of the C varies from 9.78% to 12.15%, and for Si, it was in the range of 1.57-2.01%, and for Cr, it was in the range of 35.22-50.31%, and for Mo, it was in the range of 0.56-0.70%. The weight percentage of W was observed in the range of 12.57%-20.15%, which ensures the segregation of the W. From these results, the precipitates could be inferred as $M_{23}C_6$, M_7C_3 and MC carbides.

3.2. Hardness

Figure 10 shows the hardness distribution of the surfacing layer. It can be found that the hardness of the UMCo50 substrate is the same, and the average value is about 320HV. The average hardness of the UMCo50 surfacing layer is similar to the

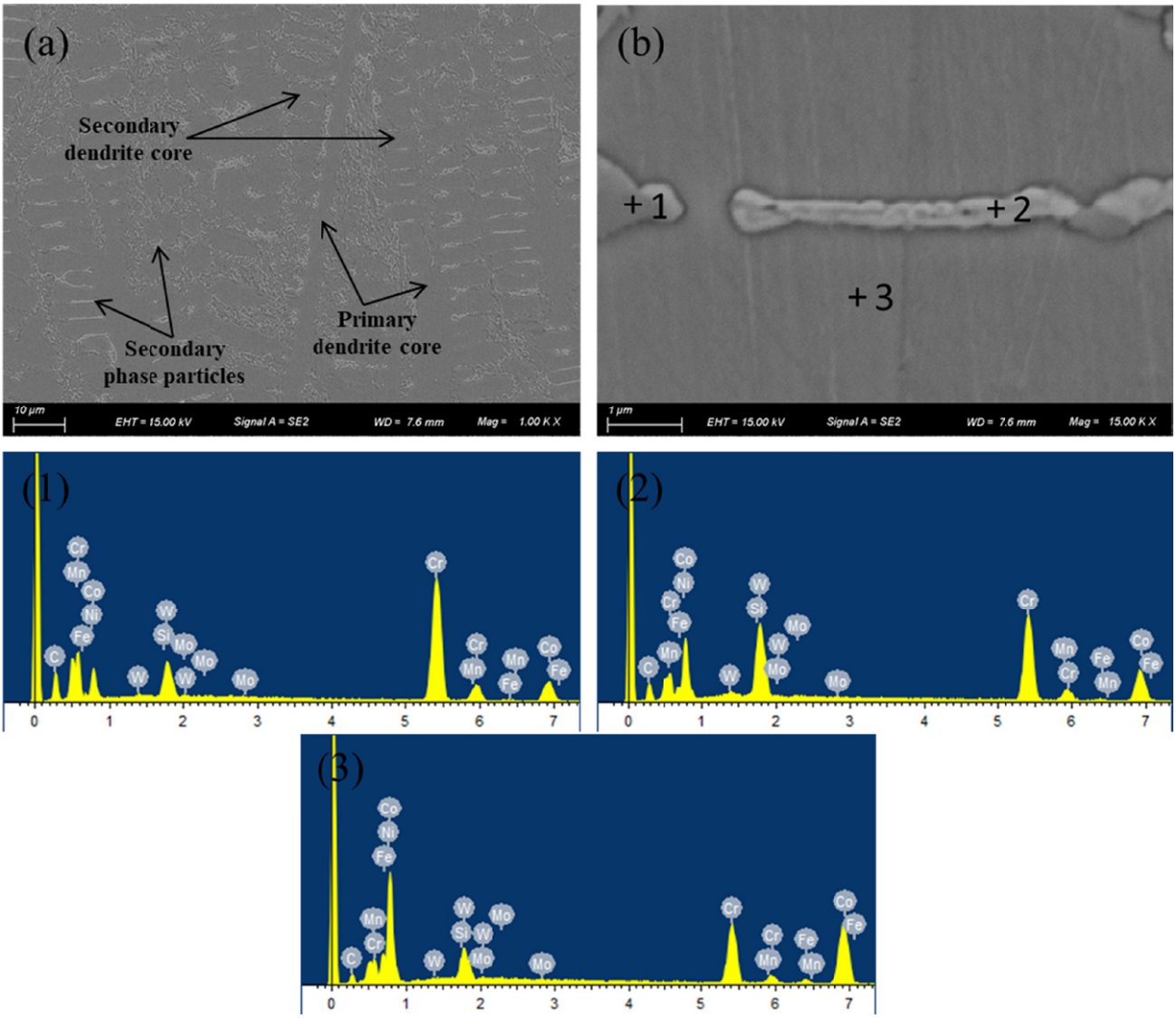

Fig. 9. (a) SEM image of the ST1 filler metal center at low magnification, (b) at high magnification showing the location for elemental composition analysis at the boundary

TABLE 6

EDS analysis results of each spot in Fig. 9(b) (wt.%)

Point	C	Si	Cr	Mn	Fe	Co	Ni	Mo	W
1	12.15	1.57	50.31	1.78	0.83	18.78	1.44	0.56	12.57
2	9.78	2.01	35.22	1.97	0.94	27.28	1.95	0.70	20.15
3	5.75	1.03	27.35	0.68	2.85	49.22	4.64	0.22	8.25

substrate. The average hardness of the ST1 and ST6 surfacing layer is 672.3HV and 497.5HV, respectively. Among them, the hardness of the ST1 surfacing layer is twice that of the UMCo50 substrate. The high hardness of the ST1 and ST6 surfacing layers is attributed to the solid solution strengthening and formation of precipitates. The difference in hardness is mainly related to the content of the C, Cr, Co and W element. During the cladding process, the W element will melt into the Co-based solid solution to form solid solution strengthening. In addition, W, Cr, Co and C can form carbides such as $M_{23}C_6$, M_7C_3 and MC. These carbides are dispersed in the matrix in the form of dots or nets, which can significantly improve the hardness of the surfacing layer. Thus, the hardness of the ST1 and ST6 surfacing layers is higher than that of the UMCo50 base metal.

3.3. High Temperature Wear Test

The high temperature wear test of the surfacing layer is carried out, and the wear loss of the surfacing layer is shown in Figure 11. The wear loss of the UMCo50 surfacing layer is 14.57 mg, and the wear loss of the ST1 and ST6 surfacing

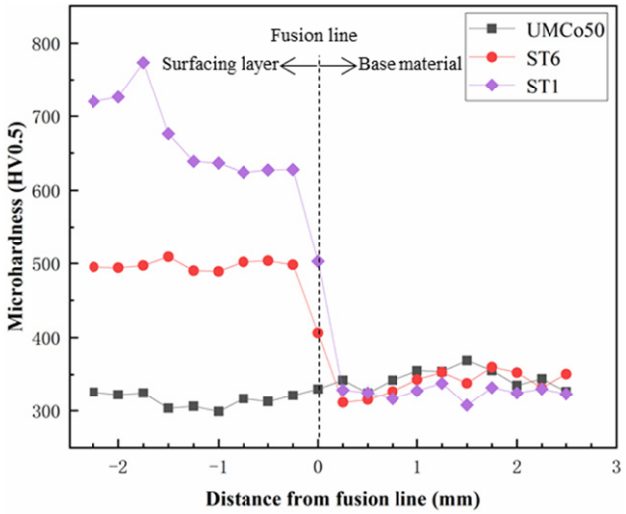

Fig. 10. Microhardness distribution of UMCo50, ST6 and ST1 surfacing layers

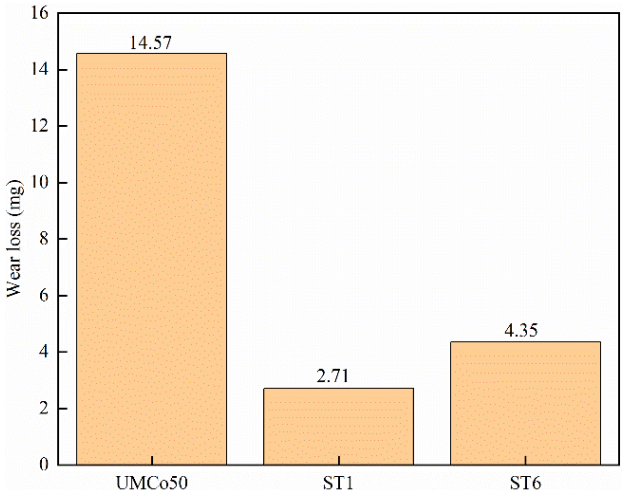

Fig. 11. Wear rates of UMCo50, ST1 and ST6 surfacing

layer is 2.71 mg and 4.35 mg, respectively. The wear loss of the ST1 and ST6 surfacing layer is lower than that of the UMCo50 surfacing layer.

According to the Archard equation [18-20], the wear amount of the surfacing layer is inversely proportional to the hardness of the surfacing layer. The hardness of the ST1 and ST6 surfacing layers is higher than UMCo50, so the wear resistance of the ST1 and ST6 surfacing layer is better than UMCo50. Also, the ST1 and ST6 welding wires have higher C content and a certain amount of W, Mn and Si elements, Mn and Si have a certain solid solution strengthening effect. W element is a carbide forming element, which can form WC with C element and distribute on the matrix. These two aspects can improve the wear resistance of the surfacing layer [21-23]. Deshpande et al. [24] found that the wear rate of Cu/WC composites is significantly higher than that of pure Cu. Zhang et al. [25] found that WC can effectively reduce the wear coefficient and help to form a transfer film during the wear process to smooth the wear track and form a stable friction layer. It can be found that the content of W and C elements has an important influence on the wear resistance of the surfacing layer. ST1 welding wire has the most W and C elements, so the surfacing layer has the least wear loss and the best wear resistance.

Figure 12 shows the coefficient of friction (COF) curve of surfacing layers. It can be found that the COF of the UMCo50 surfacing layer gradually rises from 0.21 to about 0.75 in 10 minutes, and then enters the running in period, and the COF is stable at 0.73~0.82. The COF of the ST1 surfacing layer increases from 0.16 to 0.68 in 2 minutes, and the COF is stable at about 0.35 in 13 minutes. The COF of the ST6 surfacing layer gradually rises from 0.16 to 0.68 in 5 minutes, and the COF increases slowly in 5~15 minutes, and the COF is stable at about 0.59 in 15 minutes. According to the literature [25,26], the low coefficient of friction may correspond to lower wear loss.

It can be seen from Figure 13 that the wear surface of the sample has obvious grooves along the friction direction, and obvious adhesion marks are found on the surface. The wear mechanism of the surfacing layer is mainly abrasive wear and adhesive wear. Compared with the quenched GCr15 pair of grinding discs, the hardness of the UMCo50 surfacing layer is lower and the toughness is better. When the abrasive particles move along the friction surface by tangential force, the UMCo50 overlaying layer with lower hardness will be cut or plowed by the abrasive particles, and plastic deformation will occur, grooves will be formed on the surface of the base metal. Most of the plowed surface material piled up on both sides of the furrow,

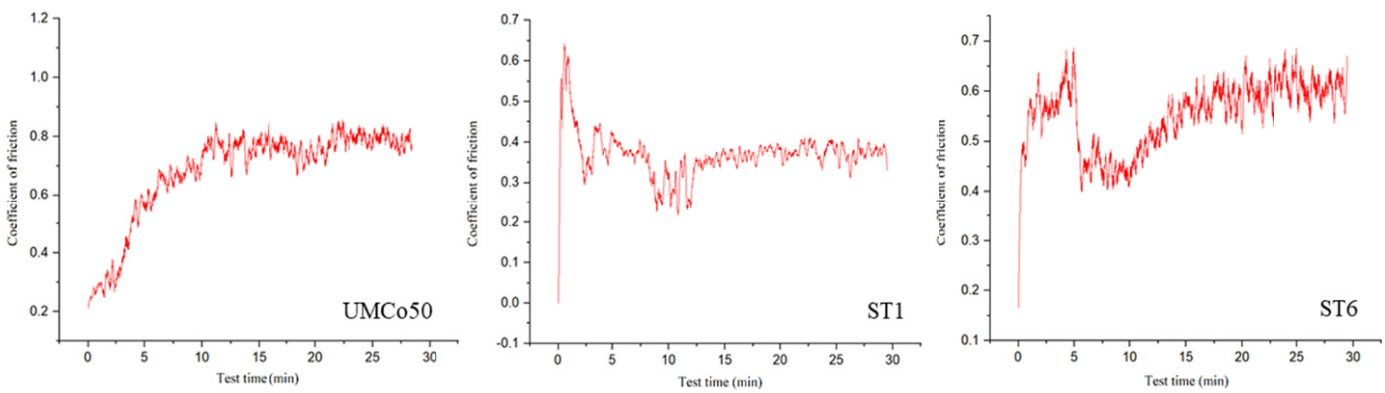

Fig. 12. Coefficient of friction curves of UMCo50, ST1 and ST6

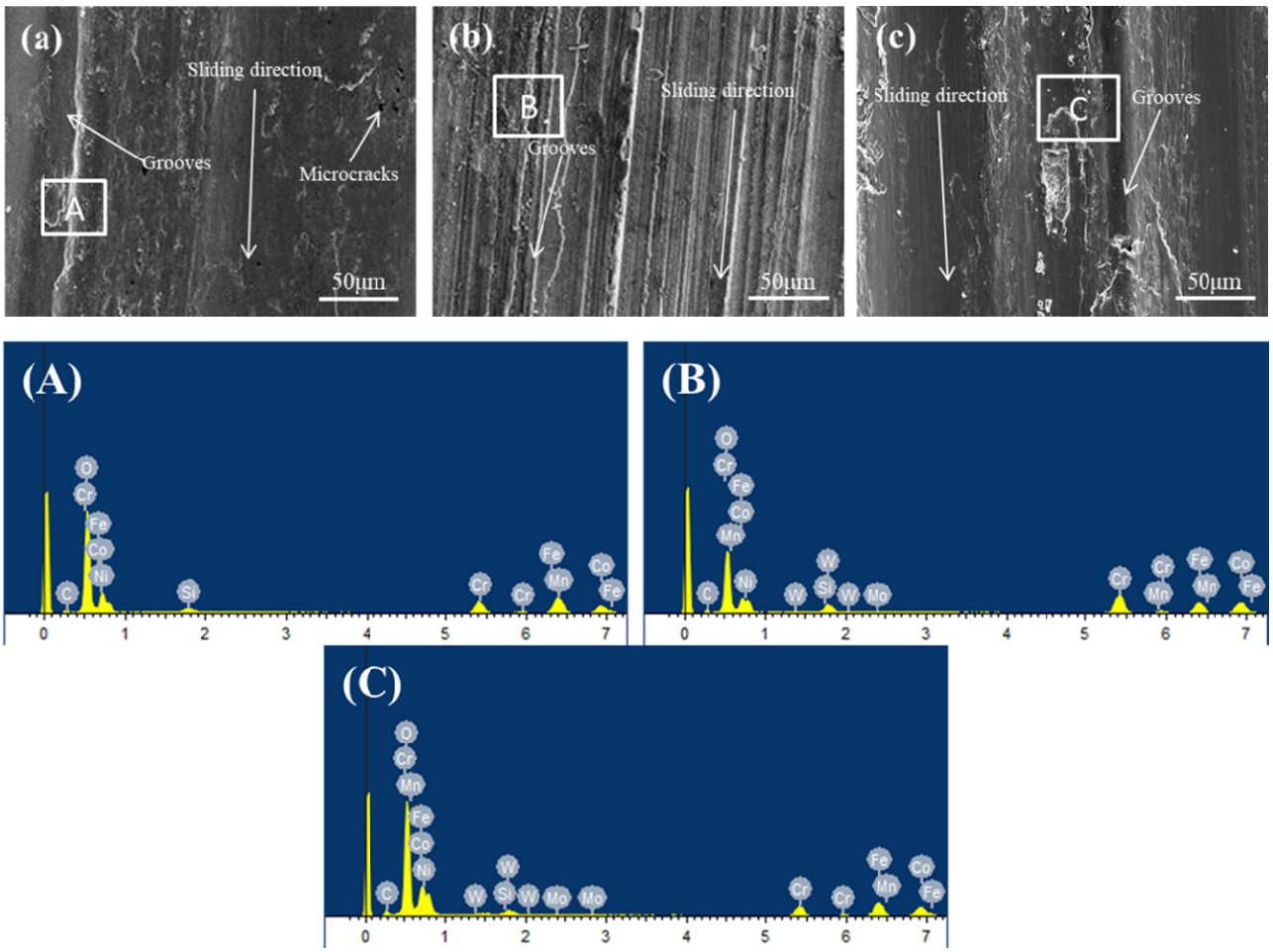

Fig. 13. SEM morphology of wear surface of the surfacing layer (a) UMCo50, (b) ST1, (c) ST6

TABLE 7

EDS analysis results of each spot in Fig. 13 (wt.%)

Point	C	Si	Cr	Mn	Fe	Co	Ni	Mo	W	O
A	2.53	0.32	13.42	0.29	29.98	18.17	1.18	—	—	34.11
B	3.70	0.96	18.83	0.74	19.98	26.16	0.95	0.17	4.94	23.57
C	5.08	0.22	15.11	0.35	22.44	20.07	2.87	0.23	2.70	30.91

and peel off under the continuous action of abrasive particles, resulting in weight loss of the surfacing layer. The wear surface of ST1 and ST6 has narrow grooves, flaking fine particles, and adhesion marks. When the grinding disc and the surface of the sample slide relatively, a part of the surfacing layer material and the oxide film formed at high temperature will peel off and form debris. These small debris will act as abrasive particles to squeeze and cut the surface of the surfacing layer, causing material loss of the surfacing layer.

The EDS results of the wear surface are shown in Table 7. It can be seen that the wear surface contains more O and Fe elements. It shows that an oxide film is formed on the wear surface during high temperature wear. The existence of the oxide film can lubricate the wear surface and have a certain inhibitory effect on the wear of the sample. However, the strength of the oxide film is relatively low, and the oxide film is likely to peel off during the wear process, exposing the material to a new surface. Repeatedly, the material is gradually lost. Therefore, the wear mechanism of the surfacing layer is abrasive wear, adhesive wear and oxidative wear.

3.4. High Temperature Corrosion

Figure 14 shows the corrosion weight loss curve of the surfacing layer in 75wt.%Na_2SO_4 + 25wt.%NaCl corrosion medium at 1000°C. It can be seen that with the increase of corrosion time, the mass loss of the surfacing layer increases, and the corrosion rate is slower initial and then faster. In the first 30 hours of the corrosion test, the slope of corrosion weight loss curve is low, which means that the corrosion rate is slow during this period. In the 30~100 h of the corrosion test, the corrosion rate increases.

The thermal corrosion process is divided into two stages: the incubation period and the expansion period. During the incubation period, a dense oxide film is formed on the surface of the surfacing layer, which can protect the alloy from further corrosion. In the expansion stage, the corrosive medium interacts with the oxide film, which makes the oxide film rupture and loses its protective effect, and the corrosion rate is accelerated. The results show that the corrosion resistance of the ST1 surfacing layer is higher than that of the ST6 and UMCo50 surfacing layers.

The corrosion morphology of the surfacing layer is shown in Figure 15. It can be found that there is a loose and porous oxide film on the surface of the UMCo50 surfacing layer, and delamination and spalling have occurred. The corrosion surface of the ST1 and ST6 surfacing layer is composed of many products with irregular shapes. In some areas, they are accumulated and agglomerated to form uneven corrosion morphology. The corrosion products of the surfacing layer are similar. The EDS

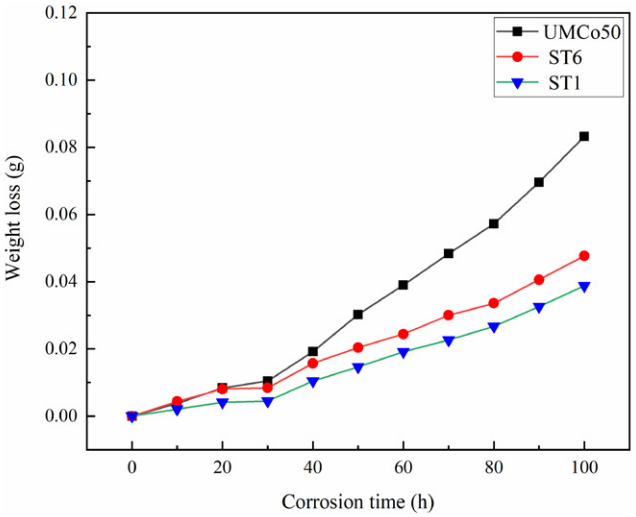

Fig. 14. High temperature corrosion weight loss of surfacing layer

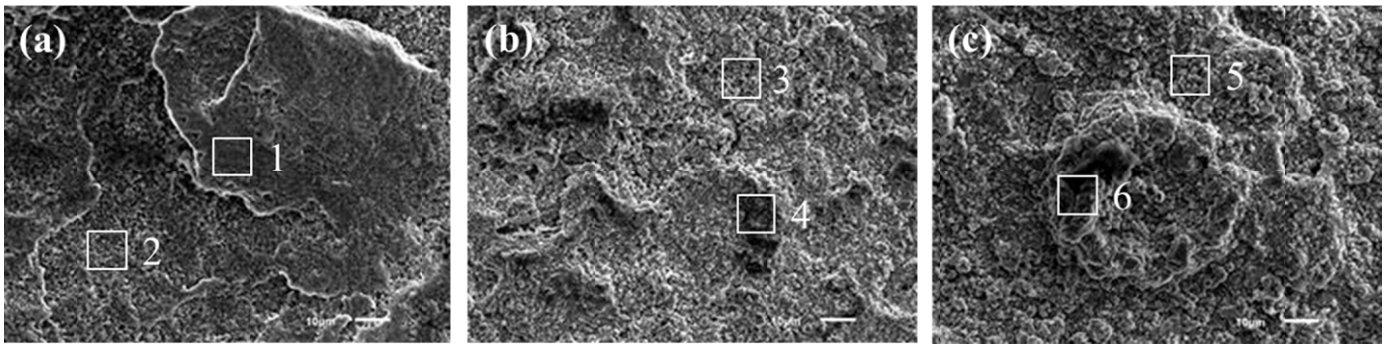

Fig. 15. Corrosion morphology of surfacing layer: (a) UMCo50, (b)ST1, (c) ST6

and XRD analysis show that the corrosion products are mainly composed of $CoCr_2O_4$, Cr_2O_3, CoO, Fe_3O_4, Fe_2O_3, and sulfide. The difference in hot corrosion resistance of the surfacing layer is mainly related to the content of Cr. The content of Cr in ST1 welding wire is the highest, it is easier to form a dense and continuous oxide film, which can better protect the base metal from corrosion damage.

TABLE 8

Element content in each area of corrosion morphology (wt.%)

Region	O	Cr	Co	Fe	Na	S	Cl
1	30.09	15.41	28.03	7.56	3.73	14.91	0.27
2	30.72	22.24	31.66	3.48	2.51	9.31	0.08
3	29.89	27.19	35.22	1.37	6.08	0.12	0.13
4	31.09	29.73	33.83	0.92	3.74	0.47	0.22
5	31.71	27.34	34.04	1.41	5.17	0.19	0.14
6	27.83	23.85	40.12	1.39	4.38	2.16	0.27

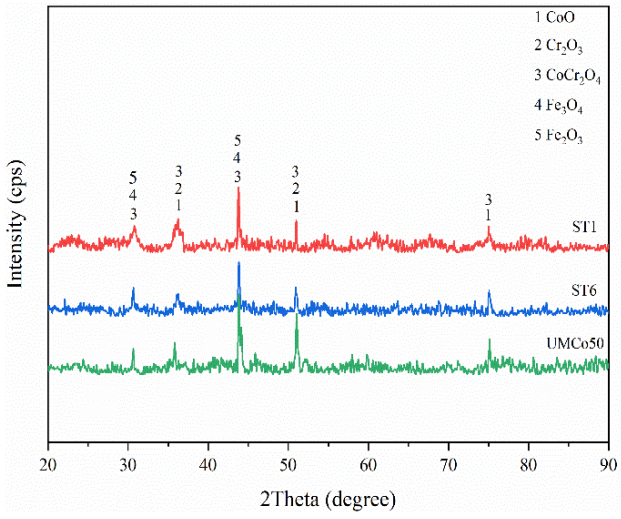

Fig. 16. XRD pattern of the surfacing layer after hot corrosion

The ST1 sample is selected for further magnification observation, as shown in Figure 17. It can be seen that the corrosion products are mainly composed of two parts, one is the spinel shape products at the bottom, and the other is the fine corrosion products without fixed shape attached to the spinel products. According to the results of the energy spectrum analysis in Table 9, it can be determined that the spinel shape products are $CoCr_2O_4$, and the fine corrosion products may be Cr_2O_3, CoO, Fe_3O_4, Fe_2O_3, and sulfide.

In the initial stage of hot corrosion, the surfacing layer contains a lot of Cr element, and Cr element has a good affinity with oxygen. Therefore, Cr_2O_3 oxide film and $CoCr_2O_4$ ($CoO{\bullet}Cr_2O_3$)

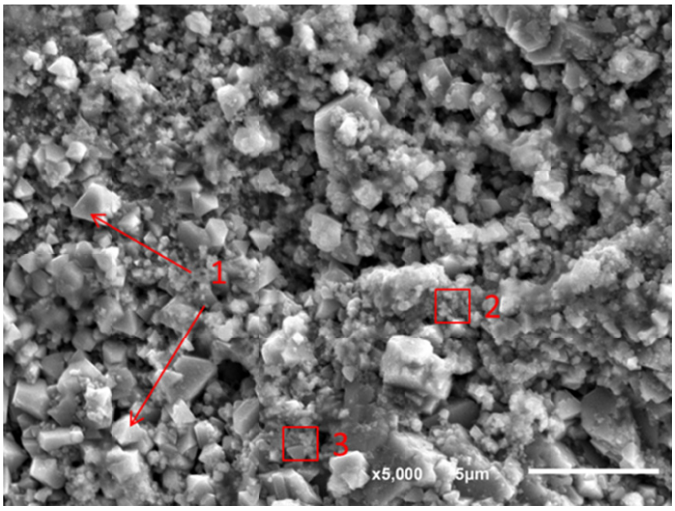

Fig. 17. Corrosion morphology of surfacing layer

TABLE 9

Element content in each area of corrosion morphology (wt.%)

Region	O	Cr	Co	Fe	Na	S	Cl
1	31.28	40.55	21.66	2.36	3.25	0.69	0.21
2	26.56	27.41	40.23	2.27	2.48	0.86	0.19
3	26.94	16.85	48.37	0.82	5.39	1.56	0.07

spinel will be formed on the surface of the sample [27]. The reaction formula is as follows:

$$2Cr + \frac{3}{2}O_2 \rightarrow Cr_2O_3 \quad (1)$$

$$CoO + Cr_2O_3 \rightarrow CoCr_2O_4 \quad (2)$$

Cr_2O_3 and $CoCr_2O_4$ oxide films can protect the matrix and prevent the corrosive medium from spreading into the matrix [28]. Under high temperature environment, NaCl will have the following reactions:

$$4NaCl + O_2 \rightarrow 2Na_2O + 2Cl_2 \quad (3)$$

With the progress of (1) and (3), the oxygen partial pressure in the salt film gradually decreases, and the following reactions will occur:

$$Na_2SO_4 \rightarrow Na_2O + SO_3 \quad (4)$$

As the reaction progresses, the content of Na_2O gradually increases, and the alkalinity of the salt film gradually increases [29,30]. The oxide film interacts with Na_2O to cause alkaline melting.

$$\frac{4}{3}Na_2O + \frac{2}{3}Cr_2O_3 + O_2 \rightarrow \frac{4}{3}Na_2CrO_4 \quad (5)$$

With the progress of the alkaline melting reaction, the dense oxide film on the surface of the surfacing layer becomes porous, which becomes a fast channel for O, S, Cl, and other elements to diffuse into the substrate, and will further accelerate the corrosion. The reaction formula is as follows:

$$Cr + Cl_2 \rightarrow CrCl_3 \quad (6)$$

$$2CrCl_3 + \frac{3}{2}O_2 \rightarrow Cr_2O_3 + 3Cl_2 \quad (7)$$

$$Na_2SO_4 + 4Co \rightarrow Na_2O + 3CoO + CoS \quad (8)$$

$$8Cr + 3SO_3 \rightarrow 3Cr_2O_3 + Cr_2S_3 \quad (9)$$

$$4NaCl + 2Cr_2O_3 + 3O_2 \rightarrow 2Na_2CrO_4 + 2CrO_2Cl_2 \quad (10)$$

Based on the above analysis, when the surfacing layer is corroded at high temperature in Na_2SO_4-NaCl molten salt medium, the high temperature corrosion forms of the surfacing layer are mainly divided into the following types: firstly, the alkaline melting of the Cr_2O_3 oxide film. The dense Cr_2O_3 oxide film on the surface of the surfacing layer becomes loose and porous, which is more conducive to the diffusion of O, S, Cl elements into the substrate to accelerate corrosion. Secondly, the sulfur element diffuses through the loose and porous oxide film to the surfacing layer to form CoS, Cr_2S_3. The generated sulfides will continue to be oxidized, and the reduced sulfur elements will continue to generate sulfides, which will aggravate the corrosion. Thirdly, the reaction of NaCl and Cr_2O_3 makes the oxide film loose and porous. At the same time, the Cl element will increase the growth stress of the oxide film and reduce the bonding strength between the oxide film and the substrate, and cause the oxide film to produce microcracks [31-33].

4. Conclusions

(1) The surfacing material is well combined with the UMCo50 base material. The microstructure of the UMCo50 surfacing layer is mainly cellular and a few columnar dendrites, the microstructure of the ST1 and ST6 surfacing layer is mainly dendrites and cellular crystals. The phases of the surfacing layer are α-Co (fcc) and ε-Co (hcp).

(2) The average hardness and wear loss of the ST1 surfacing layer are 672.3HV and 2.71mg, respectively, and the performance is better than that of the UMCo50 and ST6 surfacing layers.

(3) Under the test conditions of 1000°C, 100h, 75wt.%Na_2SO_4 + 25wt.%NaCl corrosive medium, the ST1 surfacing layer has the best corrosion resistance, and the corrosion products are $CoCr_2O_4$, Cr_2O_3, CoO, Fe_3O_4, Fe_2O_3 and sulfide.

Acknowledgement

This work was sponsored by the Natural Science Foundation of Hebei Province (E2019202407), Science and Technology Research Project of Hebei Province Colleges and Universities (Grant No. QN2019028).

REFERENCES

[1] A.J. Minchener, Coal gasification for advanced power generation, Fuel **84**, 2222-2235 (2005). DOI: https://doi.org/10.1016/j.fuel.2005.08.035

[2] J. Xiao, S.M. Wang, S.P. Ye, J.Y. Dong, J. Wen, Z.X. Zhang, Thermo-economic optimization of gasification process with coal water slurry preheating technology, Energy **199**, 117354 (2020). DOI: https://doi.org/10.1016/j.energy.2020.117354

[3] D.D. Li, J.Z. Liu, S.N. Wang, J. Cheng, Study on coal water slurries prepared from coal chemical wastewater and their industrial application, Appl. Energ. **268**, 114976 (2020). DOI: https://doi.org/10.1016/j.apenergy.2020.114976

[4] A. D. Kamble, V.K. Saxena, P.D. Chavan, V.A. Mendhe, Co-gasification of coal and biomass an emerging clean energy technology: Status and prospects of development in Indian context, Int. J. Min. Sci. Techno. **29**, 171-186 (2018). DOI: https://doi.org/10.1016/j.ijmst.2018.03.011

[5] N. Mahinpey, A. Gomez, Review of gasification fundamentals and new findings: reactors, feedstock, and kinetic studies, Chem. Eng. Sci. **148**, 14-31 (2016). DOI: http://doi.org/10.1016/j.ces.2016.03.037

[6] A. Kumar, D.D. Jones, M.A. Hanna, Thermochemical biomass gasification: a review of the current status of the technology, Energies **2**, 556-581 (2009). DOI: https://doi.org/10.3390/en20300556

[7] L.E. Taba, M.F. Irfan, W.A.M.W. Daud, M.H. Chakrabarti, The effect of temperature on various parameters in coal, biomass and CO-gasification: a review, Renew. Sustain. Energy Rev. **16**, 5584-5596 (2012). DOI: https://doi.org/10.1016/j.rser.2012.06.015

[8] H. Zhao, Y.B. Hou, H.F. Liu, X.S. Tian, J.L. Xu, W.F. Li, Y. Liu, F.Y. Wu, J. Zhang, K.F. Lin, Influence of rheological properties on air-blast atomization of coal water slurry, J. Non-Newton. Fluid. **211**, 1-5 (2014). DOI: https://doi.org/10.1016/j.jnnfm.2014.06.007

[9] D.D. Wang, S. Li, S. He, L. Gao, Coal to substitute natural gas based on combined coal-steam gasification and one-step methanation, Appl. Energ. **240**, 851-859 (2019). DOI: https://doi.org/10.1016/j.apenergy.2019.02.084.

[10] L.F. Liu, S.S. Wu, G.M. Yu, Y. Chen, Oxidation behaviour and mechanism of a cobalt based superalloybetween 1050 and 1250°C, Appl. Surf. Sci. **283**, 590-598 (2013). DOI: https://doi.org/10.1016/j.apsusc.2013.06.153

[11] H.T. Xue, D. Zhou, W.B. Guo, X.P. Luan, T. Li, J.L. Zhao, Cobalt-based alloy surfacing process optimization and surfacing material performance analysis, Mater. Res. Express. **8**, 026505 (2021). DOI: https://doi.org/10.1088/2053-1591/abdf1b

[12] D. Mutascu, I. Mitelea, I. Bordeasu, M. Burca, I.D. Utu, Hardfacing of X2CrNiMoN22-5-3 duplex stainless steel with stellite alloy using pulsed TIG welding process, Mater. Today **45**, 4112-4116 (2021). DOI: https://doi.org/10.1016/j.matpr.2020.11.662

[13] Q.Y. Hou, Z.Y. Huang, J.S. Gao, Effects of Y_2O_3 on the microstructure and wear resistance of cobalt-based alloy coatings deposited by plasma transferred arc process, Rare Metals **26**, 103-109 (2007). DOI: https://doi.org/10.1016/S1001-0521(07)60168-5

[14] J.H. Yao, Y.P. Ding, R. Liu, Q. L. Zhang, L. Wang, Wear and corrosion performance of laser-clad low-carbon highmolybdenum stellite alloys, Opt. Laser. Technol. **107**, 32-45 (2018). DOI: https://doi.org/10.1016/j.optlastec.2018.05.021

[15] W. Kurz, C. Bezenon, M. Gumann, A. Passerone, A. Columnar to equiaxed transition in solidification processing, Sci. Technol. Adv. Mat. **2**, 185-191 (2008). DOI: https://doi.org/10.1016/S1468-6996(01)00047-X

[16] J.X. Wen, H.Y. Che, R. Cao, H. Dong, Y.X. Ye, H.Y. Zhang, J. Brechtl, Y.F. Cao, P.K. Liaw, Evolution of the mechanical properties of a cobalt-based alloy under thermal shocks, Mater. Design. **188**, 108425 (2020). DOI: https://doi.org/10.1016/j.matdes.2019.108425

[17] N. Tang, Y.P. Li, P. Tunthawiroon, Y. Koizumi, A. Chiba, Thermo-mechanical fatigue test of a wrought Co-based alloy as potential tooling material for die casting, Mater. Sci. Eng. **615**, 164-168 (2014). DOI: https://doi.org/10.1016/j.msea.2014.07.073

[18] R. McCarron, D. Stewart, P. Shipway, D. Dini, Sliding wear analysis of cobalt based alloys in nuclear reactor conditions, Mater. Wear. **376-377**, 1489-1501 (2017). DOI: https://doi.org/10.1016/j.wear.2016.12.018

[19] V. Hegadekatte, S. Kurzenhauser, N. Huber, O. Kraft, A predictive modeling scheme for wear in tribometers, Tribol. Int. **41**, 1020-1031 (2008). DOI: https://doi.org/10.1016/j.triboint.2008.02.020

[20] R. Liu, D.Y. Li, Modification of Archard's equation by taking account of elastic/pseudoelastic properties of materials, Wear **251**, 956-964 (2001). DOI: https://doi.org/10.1016/S0043-1648(01)00711-6

[21] X.C. Yan, C. Chang, Z.Y. Deng, B.W. Lu, Q.K. Chu, X.C. Chen, W.Y. Ma, H.L. Liao, M. Liu, Microstructure, interface characteristics and tribological properties of laser cladded NiCrBSi-WC coatings on PH 13-8 Mo steel, Tribol. Int. **157**, 106873 (2021). DOI: https://doi.org/10.1016/j.triboint.2021.106873

[22] J. Sha, L.Y. Chen, X.T. Liu, Z.J. Yao, S. Lu, Z.X. Wang, Q.H. Zang, S.H. Mao, L.C. Zhang, Phase Transformation-Induced Improvement in Hardness and High-Temperature Wear Resistance of Plasma-Sprayed and Remelted NiCrBSi/WC Coatings, Metals **10**, 1688 (2020). DOI: https://doi.org/10.3390/met10121688

[23] J.J. Yuan, Q.Z. Wang, X.Y. Liu, S.M. Lou, Q. Li, Z.M. Wang, Microstructures and high-temperature wear behavior of NiAl/WC-Fex coatings on carbon steel by plasma cladding, J. Alloy Compd. **842**, 155850 (2020). DOI: https://doi.org/10.1016/j.jallcom.2020.155850

[24] P.K. Deshpande, R.Y. Lin, Wear resistance of WC particle reinforced copper matrix composites and the effect of porosity, Mater. Sci. Eng. A. **418**, 137-145 (2006). DOI: https://doi.org/10.1016/j.msea.2005.11.036

[25] Y.Y. Zhang, Y. Epshteyn, R.R. Chromik, Dry sliding wear behaviour of cold-sprayed Cu-MoS_2 and Cu-MoS_2-WC composite coatings: The influence of WC, Tribol. Int. **123**, 296-306 (2018). DOI: https://doi.org/10.1016/j.triboint.2017.12.015

[26] R. Liu, J.H. Yao, Q.L. Zhang, M.X. Yao, R. Collier, Sliding wear and solid-particle erosion resistance of a novel high-tungsten stellite alloy, Wear **10**, 012 (2014).
DOI: https://doi.org/10.1016/j.wear.2014.10.012

[27] M.C. Hsieh, Y.D. Ge, H. Kahn, G.M. Michal, F. Ernst, A.H. Heuer, Volatility diagrams for the Cr-O and Cr-Cl systems: application to removal of Cr_2O_3-rich passive films on stainless steel, Metall. Mater. Trans. B. **43**, 1187-1201 (2012).
DOI: https://doi.org/10.1007/s11663-012-9695-6

[28] Y. Shinata, Accelerated oxidation rate of chromium induced by sodium chloride, Oxid. Met. **27**, 315-332 (1987).
DOI: https://doi.org/10.1007/BF00659274

[29] B.P. Mohanty, D.A. hores, Role of chlorides in hot corrosion of a cast Fe-Cr-Ni alloy. Part I: experimental studies, Corros. Sci. **46**, 2893-2907 (2004).
DOI: https://doi.org/10.1016/j.corsci.2004.04.013

[30] M.A. Unsitalo, P.M.J. Vuoristo, T.A. Mantyla, High temperature corrosion of coatings and boiler steels below chlorine-containing salt deposits, Corros. Sci. **46**, 1311-1331 (2004).
DOI: https://doi.org/10.1016/j.corsci.2003.09.026.

[31] A. Zahs, M. Spiegel, H.J. Grabke, Chloridation and oxidation of iron, chromium, nickel and their alloys in chloridizing and oxidizing atmospheres at 400-700°C, Corros. Sci. **42**, 1093-1122 (2000). DOI: https://doi.org/10.1016/S0010-938X(99)00142-0

[32] R. Bender, M. Schutze, The role of alloying elements in commercial alloys for corrosion resistance in oxidizing-chloridizing atmospheres. Part I: literature evaluation and thermodynamic calculations on phase stabilities, Mater. Corros. **54**, 567-586 (2003). DOI: https://doi.org/10.1002/maco.200390129

[33] H.J. Grabke, M. Spiegel, A. Zahs, Role of alloying elements and carbides in the chlorine-induced corrosion of steels and alloys, Mater. Res. **7**, 89-95 (2004).
DOI: https://doi.org/10.1590/S1516-14392004000100013